J Mater Sci: Mater Electron
DOI 10.1007/s10854-013-1062-0

Microwave assisted hydrothermal synthesis of mesoporous SnO_2 nanoparticles for ethanol sensing and degradation

Suraj K. Tripathy · Amrita Mishra · Sandeep Kumar Jha · Rizwan Wahab · Abdulaziz A. Al-Khedhairy

Received: 5 November 2012 / Accepted: 5 January 2013

Abstract We report the synthesis of mesoporous SnO_2 nanoparticles by a microwave assisted hydrothermal process and their application as a gas sensor. The synthesized materials were characterized by transmission electron microscopy, X-ray diffraction technique, X-ray photoelectron spectroscopy, and Photoluminescence spectroscopy. As the results, we found that as-synthesized SnO_2 was synthetic Cassiterite with tetragonal structure and spherical in shape with the primary crystallite size of 6–8 nm, and the SnO_2 embedded material was mesoporous with average pore sizes of $\approx$15 nm. Moreover, this material showed excellent thermal stability from 80 to 800 °C and its crystal structure after heat treatment was preserved even at ultrahigh temperature of 800 °C. We demonstrated that this material could be used for detection of the ethanol gas because of its stability and nanoscale size at high temperature. Additionally our investigations also suggest that the processed materials can be used for the photocatalytic oxidation of ethanol. These results propose the potential application of the material for a sense and shoot kind of approach for indoor air purification in pharmaceutical and fermentation monitoring and vehicular control through breath analyzer.

1 Introduction

The ability to engineer materials on a nanometer length scale has sparked interest across many scientific disciples and has enabled direct investigation into the fundamental size-dependent properties of matter. Of the wide range of nanomaterials currently under investigation, porous metal oxides have attracted particular attention [1, 2]. Such nanostructures have been extensively studied from both experimental and theoretical viewpoints, owing to their potential applications in solar cells [3], catalysis [4], gas sensors [5], more recently in drug (and DNA) delivery [6],

Suraj K. Tripathy and Sandeep Kumar Jha previously in Department of Mechanical Engineering, Research Institute of Engineering and Technology, College of Engineering, Korea University, Seoul 136713, South Korea.

Electronic supplementary material The online version of this article (doi:10.1007/s10854-013-1062-0) contains supplementary material, which is available to authorized users.

S. K. Tripathy (✉)
Institute of Minerals and Materials Technology (CSIR), Bhubaneswar 751013, India
e-mail: tripathy.suraj@gmail.com

S. K. Tripathy · S. K. Jha
Research Institute of Engineering & Technology & Department of Mechanical Engineering, College of Engineering, Korea University, Seoul 136713, South Korea

A. Mishra
Department of Food Science and Technology, College of Agriculture and Life Sciences, Chonbuk National University, Jeonju, South Korea

S. K. Jha
Department of Bioscience and Biotechnology, Banasthali University, Rajasthan, India

R. Wahab · A. A. Al-Khedhairy
Al-Jeraisy Chair for DNA Research, Department of Zoology, College of Science, King Saud University, Riyadh 11451, Saudi Arabia

Published online: 13 January 2013

and in environmental remediation [7]. Porous materials with pore size of 2–50 nm are known as mesoporous structures and are expected to have superior properties owing to their higher pore volume and extremely high surface area. Unlike the nano and micro-porous materials, synthesis of mesostructures needs specialized skills and precise control over the processing parameters. The most common approaches are sol–gel processing [8], surfactant assisted synthesis [9], precipitation technique [10] etc. However, the materials obtained via these techniques are poorly crystalline and may contain organic impurities. Post synthesis by heat treatment can enhance the crystallinity and also help to remove the organic impurities. However, there exists a strong possibility of severe particle aggregation and grain growth, which may reduce the potential of such materials in devices like gas-sensors and solar cells [11]. Hence, researchers are continuously trying to develop other synthetic processes such as hydrothermal processing, microwave assisted synthesis etc. to obtain well crystalline mesostructures. Periyat et al. [12] has synthesized TiO_2 mesostructures via microwave heating for electrochromic displays. Similarly, Lee and Song [13] has reported hydrothermal synthesis of anatase TiO_2 mesostructures. In spite of the high potential applications of mesostructures, most of the work has been concentrated on SiO_2, TiO_2, and zeolites. SnO_2 is an n-type semiconductor with a large band-gap [14], and is well known for its applications in photocatalysis [15], gas sensors [16], and dye-based solar cells [17]. Recently, hollow microspheres of tin dioxide have received much attention for water treatment [18]. However, very few reports are available on the synthesis of mesoporous nanostructures of SnO_2. One of the most successful attempts was reported by Demir-Cakan et al. [19]. They have obtained mesoporous SnO_2 microspheres by hydrothermal carbonization. Their material showed good crystallinity, which they applied for lithium ion based charge storage. Unfortunately, this process has not been exploited to obtain nanoparticles. Fujihara et al. [20] has proposed a hydrothermal route for the synthesis of mesoporous SnO_2 nanoparticles which are stable up to 200 °C. However, gas-sensor applications need materials with higher thermal stability. The qualified synthesis of mesoporous nanoparticles is considered to be much more difficult than their micron size counterparts. The presence of larger pore sometimes makes the material unstable and thus makes the process difficult. Microwave assisted hydrothermal (M–H) technique has received importance due to its precise temperature control, high reaction rate, scale-up capability and arguably superior product quality [21]. Recently, Krishna and Komarneni [22] have synthesized SnO_2 particles with the size range of 3–9 nm by using $SnCl_4$ as the source material. However, these methods have not been used to produce porous structures. Thus, the formation of porous SnO_2 nanoparticles via M–H technique still remains a challenging issue.

In the present paper, we report a facile M–H synthesis technique to obtain well–crystalline SnO_2 mesoporous particles with crystallite size of 6–8 nm by using sodium hexahydroxostannate as the source material. Formation of nanoparticles was confirmed from transmission electron microscopy (TEM) images and crystal structure of the material was investigated by the X-ray diffraction (XRD). As-synthesized material was mesoporous in nature with an average surface area of 65 m^2/g. The material has shown excellent thermal stability in the range of 80–800 °C. Mesoporous SnO_2 nanoparticles were investigated as a candidate material for thick film based ethanol-sensor. Additionally they have shown interesting photocatalytic property for oxidation of ethanol. Our investigations demonstrate the potential of this material in designing a sense and shoot kind of device for indoor air purification.

2 Experimental

2.1 M–H synthesis of SnO_2 nanoparticles

In a typical process; 0.1 M of sodium hydroxide solution was added drop wise to known amount of 40 mM of sodium hexahydroxostannate (Sigma) until the pH = 10.5 was achieved. Then the solution was transferred to a Teflon reactor. The reactor was sealed and placed in the microwave oven (CEM Mars 5) and heated at 150 °C for 30 min. After the reaction was over, the reactor was allowed to cool as the natural process. Then the materials were collected by centrifugation technique at 10,000 rpm. The samples were washed with deionized water to remove the impurities. The samples were dried at 80 °C for 12 h in a dry oven and used for analysis. The morphology of the nanoparticles and nanoparticle films was investigated by TEM (JEOL-JEM-2010). The crystal phase of the nano-composite films was investigated by XRD technique (D/Max 2005, Rigaku). Optical properties have been investigated by photoluminescence spectroscopy. X-ray photoelectron spectrum was collected to understand the surface state of the synthesized nanoparticles (AXIS-NOVA, Kratos). SnO_2 samples were also prepared via normal hydrothermal technique and procured commercially (Hefei Quantum Quelle Nano Science and Technology Co., Ltd, 99.5 %) for comparing their sensing and photocatalytic activity with that of newly synthesized materials.

2.2 Fabrication of thick film based sensing device and sensing tests

SnO_2 paste was prepared by dispersing the SnO_2 powder in isopropyl alcohol with hydroxylpropyl cellulose (HPC) of

one half of the SnO_2 powder weight using an ultrasonic disperser for 20 min. For enhancing the specificity of sensor, 0.05 wt% platinum was doped into the materials prior to the processing of paste. The paste was deposited on the commercial Al_2O_3 substrate (15 mm × 15 mm) with previously screen printed platinum electrodes (10 mm × 10 mm) by doctor blade technique and dried at 200 °C for 1 h followed by baking in a furnace at 400 °C for 1 h. The ethanol-sensing activity of the device was investigated by using a homemade gas-sensing evaluation system (supplementary Figure. 1) equipped with digital mass flow controllers, rapid heating system with programmed temperature controller, and quartz reactor for carrying out the sensing reactions. The change in resistance of the device due to the presence of target gas was measured using a high resistance meter (Keithley source meter 2400). The device was tested in the temperature range of 50–400 °C at various concentrations of target gas (5–500 ppm) in a temperature-controlled environment. The background gas was N_2, mixed with atmospheric air to have 10 % of oxygen content. The flow of gas (100 mL/min) over the sensor device was altered between the sample gas and dry air to record the sensor response in terms of electric resistance. The sensor response was represented as the relative change in the resistance of the device in the presence of air and target gas according to following equation;

$$\text{Sensor response} = R_{air}/R_{gas}$$

where R_{air} and R_{gas} are the resistance of the device in presence of dry air and the target gas respectively.

2.3 Evaluation of photocatalytic activity

Photocatalytic tests were carried out by using gas chromatography technique (Shimadzu GC-2010 series). A sketch of the gas-chromatography arrangement for the evaluation of photocatalytic activity is given in supporting materials. A thick film (≈500 nm) of the SnO_2 nanopowder was deposited onto glass plate (5 cm × 5 cm) as explained above. Ethanol gas (50–500 ppm) was used to investigate the photocatalytic activity of the samples. Irradiations were carried out using two UV-365 nm lamps (15 W). Prior to evaluation, blank experiments were carried out to confirm the possible reactions occurring in the absence of catalyst or UV-light.

3 Results and discussion

The morphology of the as synthesized materials is investigated by TEM and images are shown in Fig. 1a–d. As shown in Fig. 1a, b, the SnO_2 primary nanoparticles were spherical in shape with the crystallite size of 6–8 nm. Oxide nanoparticles were found to have inter-planar spacing of 0.267 nm, which corresponds to the (101) plane of the cassiterite SnO_2 with tetragonal geometry. Figure 1d shows the electron diffraction pattern of the as synthesized material. The ring patterns were found to be in good agreement with the (110), (101), and (211) planes of the cassiterite SnO_2.

In order to know the structural behavior of the material, the crystal structure was investigated by powder XRD technique. XRD patterns of the SnO_2 nanoparticles heat treated at various temperatures (80–800 °C) for 2 h are shown in Fig. 2a. As-prepared material was found to be crystalline with four distinct peaks at 26.2, 33.8, 51.4, and 65.1 nm corresponding to (110), (101), (211), and (112) planes of the Cassiterite SnO_2. The crystalline nature increased with increase in the heat treatment temperature [23]. Few minor additional planes of tetragonal SnO_2 becomes clearly visible with increase in the heat treatment temperature. However, the crystal structure and phase of the material remains unchanged. Mean crystallite diameter (MCD) of the material is calculated by using Scherrer's formula and summarized in Fig. 2b. It is observed that the material dried at 80 °C after the synthesis has MCD ≈7.8 nm. With increase in the heat treatment temperature up to 200 °C, MCD value increased to 10.5 nm. Up to 700 °C, the MCD did not change remarkably and remained close to 11 nm. When the heat treatment temperature is increased to 800 °C, an increase in the MCD value (≈12 nm) is noticed. Thus we can suggest that the MCD value changed from 8 nm to 10 nm with increase in the heat treatment temperature from 80 to 700 °C. Similarly the effect of heat treatment time at 400 °C on the MCD is also calculated and shown in Fig. 2b. It is observed that the MCD did not change remarkably even after 24 h of heat treatment. These results suggest that the SnO_2 nanoparticles synthesized by M–H technique have excellent stability at higher heat treatment temperature and hence can be used as efficient gas-sensing material.

The optical property of the as synthesized materials is investigated by photoluminescence and UV–visible spectroscopy. Figure 3a shows the room-temperature photoluminescence spectrum of as prepared SnO_2. Two peaks, one centered in the UV band at 380 nm (3.26 eV) and another broad peak centered in the green band at 520 nm (2.38 eV) are observed. Since the emission maxima (380 and 520 nm) are both lower than the band gap of the SnO_2 nanocrystal, about 4.1 eV, the visible emission could not be assigned to the direct recombination of a conduction electron in the Sn 4p band and a hole in the O 2p valence band. The peak at 520 nm might be originated from the luminescence centers formed by tin interstitials or dangling in the present SnO_2 nanoparticles, but the exact mechanism

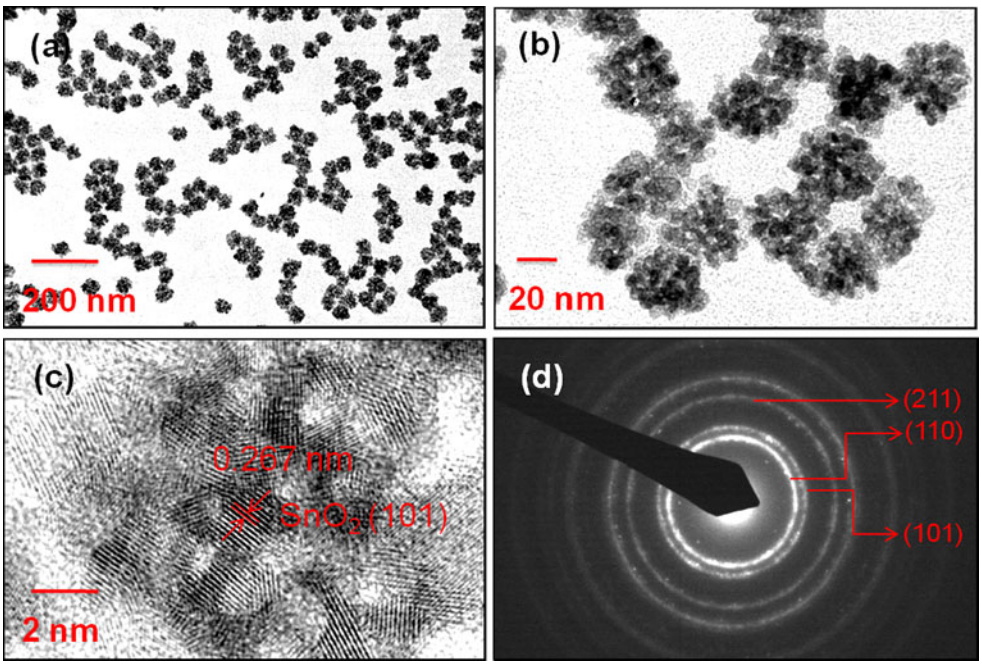

Fig. 1 TEM (**a**, **b**), HRTEM (**c**), and SAED (**d**) images of SnO_2 nanoparticles synthesized via M–H technique

remains unclear at present [24]. The emission at 380 nm was expected to be due to electron transition mediated by defects levels in the band gap, such as oxygen vacancies. In the SnO_2 nanoparticles, the intrinsic defects, such as oxygen vacancies, which act as luminescent centers, could form defect levels located highly in the gap, trapping electrons from the valence band to make a contribution to the luminescence [25]. Generally, in poly- and nano-crystalline oxides, oxygen vacancies are known to be the most common defects and usually act as radiative centers in luminescence processes. Also, the oxygen vacancies could be present in three different charge states: O^0, O^+, and O^{2+}. The oxygen vacancy is an intrinsic donor in SnO_2. Because O^0 is a very shallow donor, it was expected that most oxygen vacancies would be present in their paramagnetic O^+ state under flat-band conditions [26, 27]. Similar observations in quantum nanoparticle systems had been reported in the literature [28]. However, the detailed explanations are still under investigation. Figure 3b shows the UV–visible spectrum of the aqueous dispersion of the as synthesized nanoparticles. From this figure it is observed that the spectrum shifts sharply at 320 nm which indicates that the material may have band gap of 3.8 eV [29].

The survey XPS spectrum of the as synthesized SnO_2 nanoparticles is shown in Fig. 4a. The survey indicates that the nanoparticles are mainly composed of Sn and O. Small peaks due to Na and C are also observed. The point of zero charge for SnO_2 is about pH 4. At pH 10, the particles have a large excess negative charge due to ionization of surface hydroxyl groups. Drying the samples for XPS measurements leads to the condensation of counter ions, which in this case are sodium ions. However some sodium may precipitate as Na_2CO_3. This is confirmed by the XPS results. There are clear peaks due to the C 1s transitions, which indicate the presence of excess carbon in the material [30]. An alternative explanation for this mechanism can also be expected. The excess carbon may also be expected to have its origin from the residual citrate ions in the reaction solution. Minor peaks due to Si are also detected, which may have entered during sample preparation, since silica in reaction vessels is solubilized above pH 9. The samples exhibit two Sn $3d_{3/2}$ (495.4 eV) and Sn $3d_{5/2}$ (484.0 eV), which indicates the tin is predominantly in the Sn^{4+} state (Fig. 4b). The XPS spectrum of O 1s of the core–shell nanocomposite is observed at 531.6 eV (Fig. 4c). On the basis of this result a simple formation mechanism could be expected for this synthesis procedure. During the reaction, sodium hexahydroxostannate reacts with atmospheric CO_2 and water in alkaline medium to form a gelatinous colloid of SnO_2 (arguably hydrous tin dioxide) [31]. The chemical equation involved is given as;

$$Na_2SnO_3 + H_2O + CO_2 \rightarrow Sn(OH)_4 + Na_2CO_3 \quad (1)$$

Heating at 150 °C promotes dehydration of the initial hydrated gel to form crystalline tin dioxide as per mechanism given in Equation-2.

$$Sn(OH)_4 \rightarrow SnO_2 + 2H_2O \quad (2)$$

Metal oxides are generally more resistant than other colloids to coagulation due to the formation of an

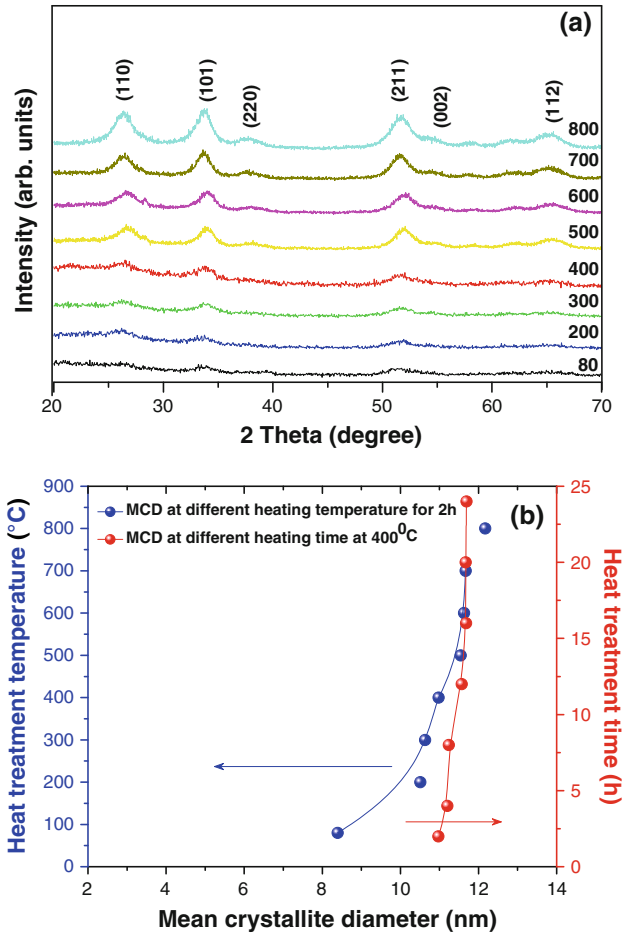

Fig. 2 **a** XRD patterns of SnO_2 nanoparticles synthesized via M–H technique and heat treated for 2 h at different temperatures, **b** increase in the mean crystallite diameter of the SnO_2 nanoparticles with respect to heat treatment temperatures

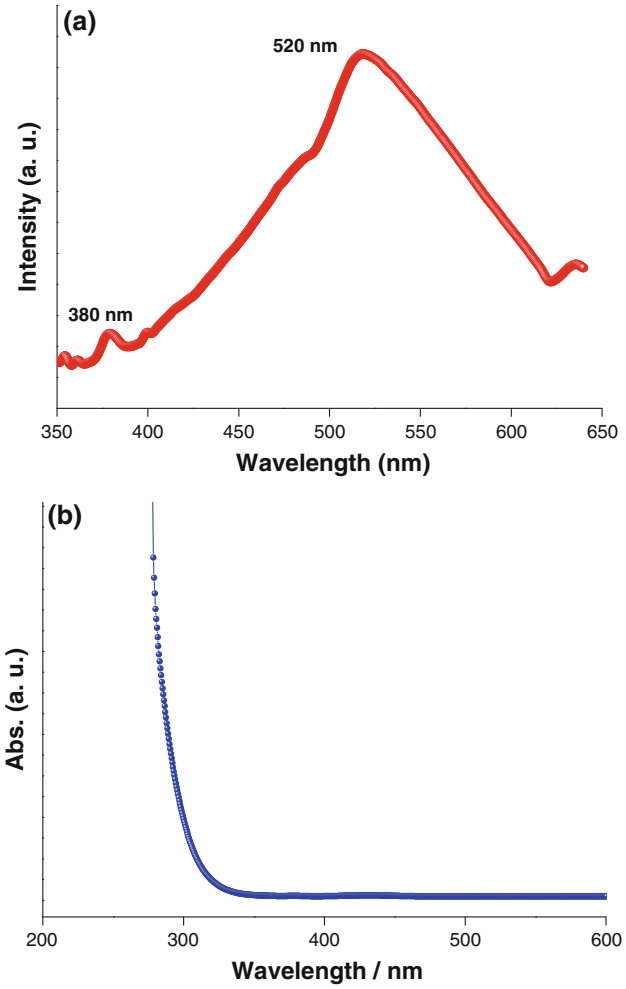

Fig. 3 **a** Photoluminescence and **b** UV–visible spectrum of SnO_2 nanoparticles synthesized via M–H technique

electrosteric barrier at the particle surface [32]. It is important to control the coagulation of nanoparticles to produce large nanoclusters with uniform size distribution. In the present case the pH was expected to be the key factor in the synthesis of well-dispersed nanoclusters due to inter-particle interaction.

The adsorption–desorption isotherm plot for the nitrogen sorption (77 K) of the SnO_2 sample that was synthesized by M–H technique and dried at 80 °C for 12 h shows typical behavior (Fig. 5). The plot corresponds to the "type IV" isotherm in the Brunauer classification [33]. A hysteresis loop observed in the plot is associated with the filling and emptying of mesopores (pores of diameter 2–50 nm) by capillary condensation. Furthermore, the loop was found to be of "type H-2" associated with an interconnected network of pores of different shapes. Closure of the loop at P/P_0 (relative pressure) of 0.5 indicates the presence of very small pores [33]. Pore size distributions were then determined by the BJH method applied to the adsorption branch in the plot. A typical pore size distribution for the SnO_2 sample is shown in inset of Fig. 5. The sample exhibited average pore size in the range of 15–20 nm indicating the mesoporous nature of the material. The specific surface area of SnO_2 samples was evaluated to be 65.5 m^2/g based on the BET result. This high surface area and mesoporous nature is expected to be very beneficial for adsorbing gas and other molecules [6, 34, 35].

Further, as-synthesized nanoparticles were deposited on the alumina substrate with platinum electrode and heat treated for ethanol-sensing experiments. The SEM images of the tin dioxide films confirmed granular form of SnO_2 without any significant aggregation (Supplement figure 2), which is a suitable condition for gas sensing application. The ethanol-sensing activity of the device was investigated by using a homemade gas-sensing evaluation system. Figure 6a, b shows the sensor response for ethanol and recovery time at different operating temperatures respectively. Sensor response for ethanol was measured at 5, 10, 25,

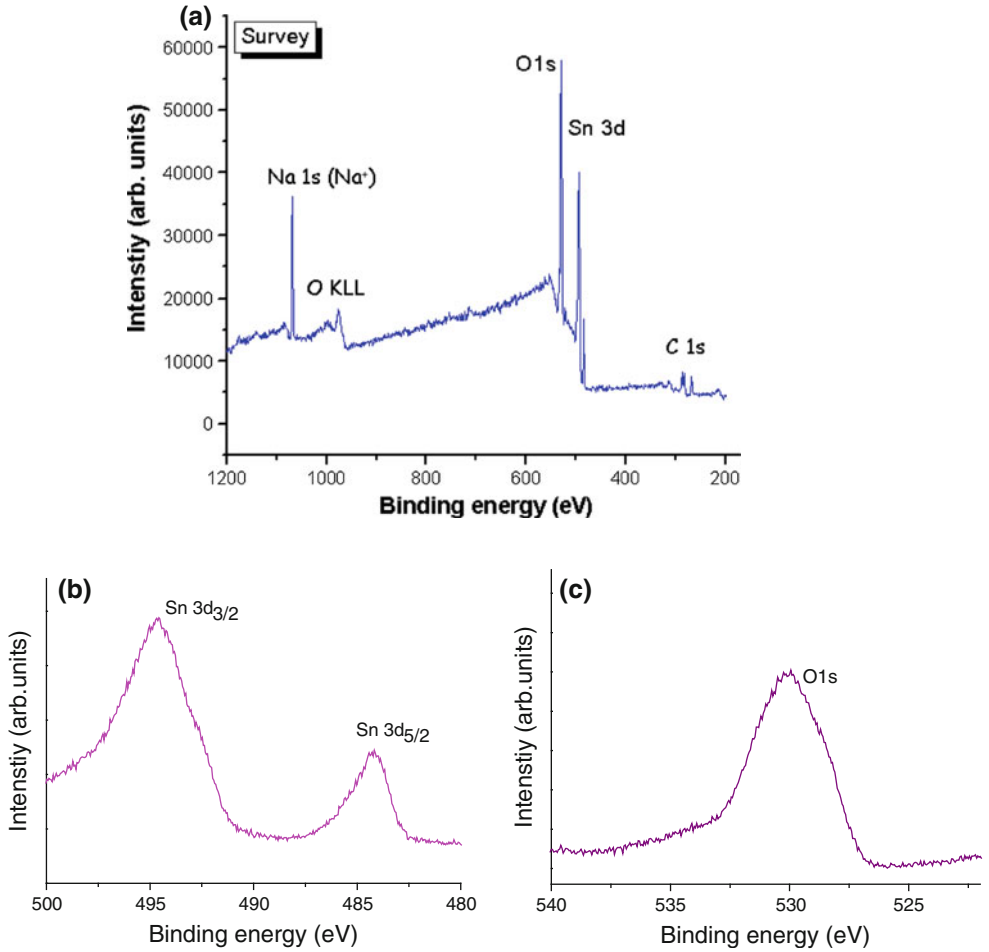

Fig. 4 XPS of SnO_2 nanoparticles synthesized via M–H technique

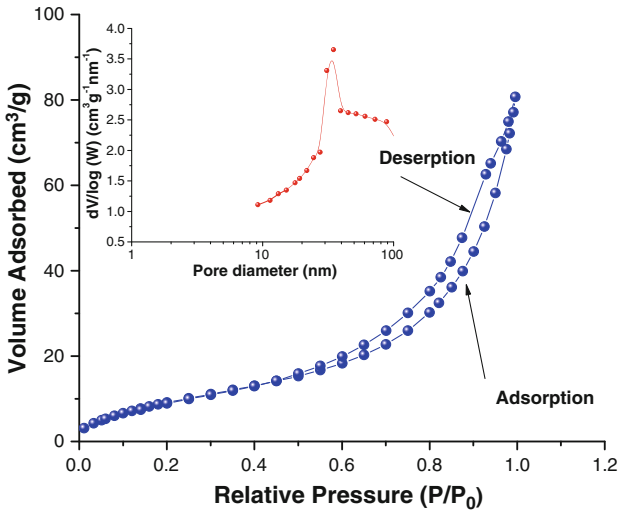

Fig. 5 Nitrogen adsorption/desorption isotherms obtained at 77 K and inset shows the pore size distribution of the as-synthesized mesoporous SnO_2

50, 100, 200, and 500 ppm concentrations. The highest sensitivity (for 200 ppm of ethanol) of 58.6/ppm was observed at 350 °C in the linear range. The inset to Fig. 6a explains the sigmoidal behavior of sensor response in the form of calibration curve at 350 °C. The sensor had a response time of ≈18 s, linear detection range ($y = 0.331x + 1.898$, $R^2 = 0.94302$) between 5 and 200 ppm (inset to Fig. 6a) (comparable with previous literature [36]) and an experimentally calculated limit of detection (LOD) of 2.5 ppm of ethanol (LOD was calculated as over three times the standard deviation of sensor response for minimum detectable concentration). The response time for the sensing device was 18 s (Supplement figure 4a). The recovery time for the sensor was 10–150 s for different concentrations of ethanol (Fig. 6b; Supplement figure 4a). A recovery time of 50–100 s is generally acceptable for similar gas sensors [37, 38]. The sensor also showed excellent reproducibility (>94.6 ± 1.25 %) for concurrent measurements and recoveries (Supplement figure 4b).

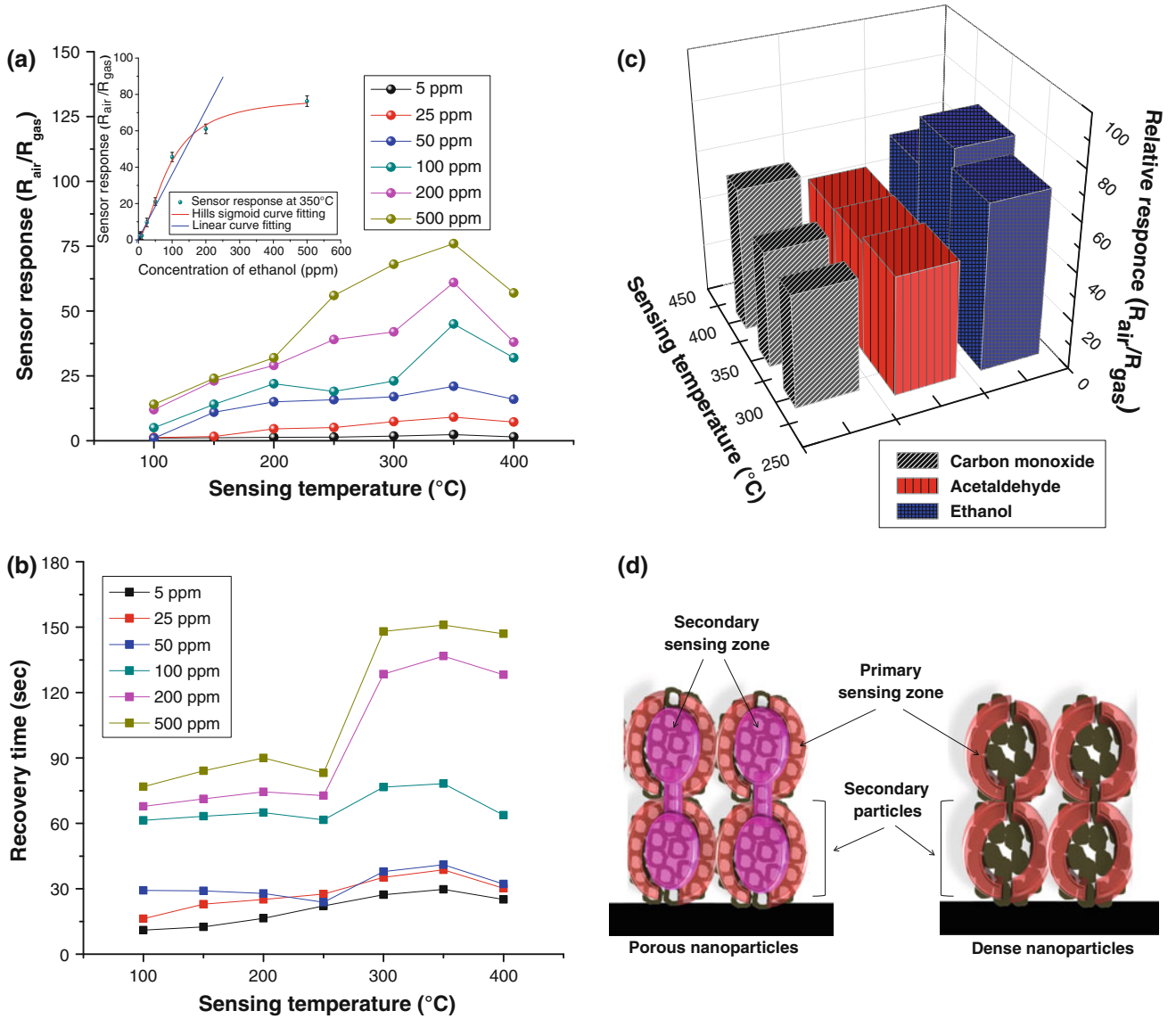

Fig. 6 **a** Ethanol sensing by the sensing device at different operating temperature, **b** recovery time for ethanol sensing, **c** Sensitivity at 350 °C for different concentration of ethanol **d** Difference between sensing mechanism on porous and dense nanoparticles

The interfering gases such as acetaldehyde (Supplement figure 3a) and carbon monoxide (Supplement figure 3b) also produced a detectable sensor response at equivalent concentration to ethanol, yet, the sensor response was temperature specific (Fig. 6c). It is a well known fact that similar gas sensors [37], or others, for example, CO_2 sensor based fire alarms based on thick or thin film oxides do have cross reactivity towards various other gases, however, if set under optimum operational conditions, they perform adequately in test conditions [39]. Moreover, one of the merits of our detection system was the enhanced sensitivity towards target analyte (Fig. 6d), as porous structures provide additional (or secondary) sensing zone which is expected to absorb more oxygen species and hence contributes to enhance the sensitivity of the material [40, 41]. Dense particles will obviously lack this secondary sensing zone and hence will have lesser adsorption sites for oxygen species which will reduce their sensing ability. In addition to the porous structure the crystal structure and average grain size is expected to have significant role in preserving the sensing ability of the device. The high thermal stability of the material at higher heat treatment temperature is one of the most interesting features of the present synthetic protocol. It is well known that the SnO_2 particles with an average grain size of 10 nm can arguably have optimum gas sensing activity under a given test condition [35]. Thus it is expected that the present synthetic protocol can produce SnO_2 nanoparticles which is not only highly crystalline but also thermally stable over a wide range

of temperature. An experimental justification to this argument is obtained by comparing the ethanol sensing activity of SnO_2 samples prepared by different techniques and obtained from commercial source (supporting materials figure 5).

In addition to gas-sensing, SnO_2 nanoparticles with higher surface area are expected to have interesting photocatalytic properties [42]. Thus, we investigated the photocatalytic activity of our device on ethanol samples with the aim of developing sense and shoot strategy for indoor air purification, keeping in view the health hazards posed by workers in ethanol industry. The photocatalytic oxidation of ethanol was monitored using gas-chromatography technique. The results are shown in Fig. 7a. It was observed that ethanol gas was almost completely oxidized to carbon dioxide within 60–90 min. For SnO_2 with the band gap energy of 3.8 eV (close to that of TiO_2), theoretically it can be excited by the photons with the wavelengths under 490 nm. However, pure tin dioxide in known to have less photocatalytic activity. This is probably due to the faster recombination of the photogenerated electron/hole pairs in SnO_2 [42]. However, in case of noble metal-doped (Pt in the present case) SnO_2, following situation is expected. Since SnO_2 (similar to TiO_2) undergoes charge separation under UV-irradiation, the photogenerated electrons are expected to be transferred to noble metal nanoparticles as both systems undergo charge equilibration. The transfer of electrons from the excited semiconductor to the metal is an important aspect that dictates the overall energetic of the composite and hence the efficiency of photocatalytic reduction process. The photoactive SnO_2 thus, plays an important role of absorbing incident photons and injecting electrons into the noble metal surfaces. The processes that lead to storing of electrons in the noble metal core are summarized below (reactions 3–5) and in Fig. 7b.

$$SnO_2 \rightarrow SnO_2(e^- + h^+) \tag{3}$$

$$SnO_2(h^+) + \text{Ethanol} \rightarrow \text{Products} \tag{4}$$

$$SnO_2(e^-) + \text{metal} \rightarrow SnO_2 + \text{metal}(e^-) \tag{5}$$

Under UV excitation, SnO_2 undergoes charge separation followed by charge recombination and interfacial charge-transfer processes. As the photogenerated holes are scavenged by acetaldehyde, the electrons accumulate within the SnO_2 particles. Since metal particles such as palladium with a favorable Fermi level are good electron acceptors, we expect a facile electron transfer from excited SnO_2. This property of charge equilibration between semiconductor and metal nanoparticles has been suggested by Kamat et al. [42] by the addition of metal colloids to preirradiated TiO_2 colloids in ethanol. In the present case the mechanism is expected to be similar to that suggested by Kamat et al. [42]. Thus presence of the smaller noble metal core is expected to enhance the photocatalytic activity of the tin dioxide.

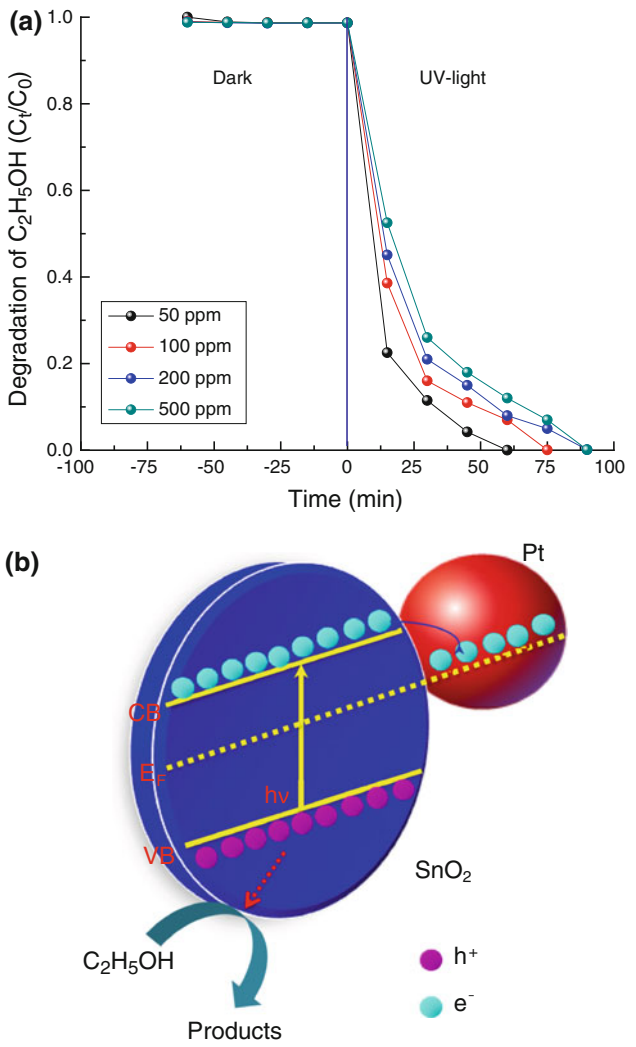

Fig. 7 **a** Photocatalytic degradation of ethanol over SnO_2 mesostructures containing Pt, **b** mechanism of photocatalytic degradation of ethanol over SnO_2 mesostructures containing Pt

Therefore, the results above provide an interesting opportunity for the design of a sense and shoot kind of device for indoor purification. The first report of such kind of system in an aqueous medium was proposed by Kamat et al. [42]. Our investigations provide an initial approach to the realization of such a system for detection and degradation of ethanol. The developed method also has the applicability in pharmaceutical and fermentation monitoring and vehicular control through breath analyzer [43]. Apart from that, it can be used to sense acetaldehyde and CO however at much lower sensitivity than for ethanol.

4 Conclusion

In summary, a microwave assisted hydrothermal technique was reported for synthesis of mesoporous SnO_2 nanoparticles

at 150 °C. XRD has showed that the as-prepared sample is synthetic Cassiterite with tetragonal structure. TEM has confirmed that the SnO_2 nanoparticles are spherical in shape with the crystallite size of 6–8 nm. As synthesized nanoparticles has shown defect mediated luminescent peaks in the UV (380 nm) and green (520 nm) region. The material has shown excellent thermal stability till 800 °C which makes it suitable for gas-sensor applications. The materials have shown highest ethanol-sensing at 250 °C. Additionally the materials have shown good photocatalytic activity for the oxidation of ethanol. Our investigations demonstrate the possible application of the materials for detection and degradation of volatile organic compounds via a sense and shoot approach. In addition to this the developed materials also has the applicability in pharmaceutical and fermentation monitoring and vehicular control through breath analyzer.

References

1. P. Behrens, Angew. Chem. Int. Ed. Engl. **35**, 515 (1996)
2. U. Ciesla, F. Schüth, Microporous Mesoporous Mater. **27**, 131 (1999)
3. L. Li, C. Liu, J. Phys. Chem. C **114**, 1444 (2010)
4. A. Taguchi, F. Schüth, Microporous Mesoporous Mater. **77**, 1 (2005)
5. V. Nechita, J. Schoonman, V. Musat, Phys. Status Solidi A **209**, 153 (2012)
6. F. Torney, B.G. Trewyn, V.S.Y. Lin, K. Wang, Nat. Nanotech. **2**, 295 (2007)
7. P. Misaelides, Microporous Mesoporous Mater. **144**, 15 (2011)
8. K. Niesz, P. Yang, G.A. Somorjai, Chem. Comm. **2005**, 1986 (2005)
9. L. Wang, Z. Wang, J. Zhao, Z. Yuan, H. Yang, M. Zhao, Mater. Chem. Phys. **59**, 171 (1999)
10. J.W. Park, D.S. Jung, M.E. Seo, S.Y. Kim, W.J. Moon, C.H. Shin, G. Seo, Microporous Mesoporous Mater. **112**, 458 (2008)
11. C.N.R. Rao, A. Govindaraj, S.R.C. Vivekchand, Ann. Rep. Prog. Chem. A **102**, 20 (2006)
12. P. Periyat, N. Leyland, D.E. McCormack, J. Colreavy, D. Corr, S.C. Pillai, J. Mater. Chem. **20**, 3650 (2010)
13. K.H. Lee, S.W. Song, Appl. Mater. Interface **3**, 3697 (2011)
14. M. Batzill, U. Diebold, Prog. Surf. Sci. **79**, 47 (2005)
15. S. Wu, H. Cao, S. Yin, X. Liu, X. Zhang, J. Phys. Chem. C **113**, 17893 (2009)
16. R. Triantafyllopoulou, C. Tsamis, Phys. Status Solidi A **205**, 2643 (2008)
17. J.H. Lee, N.G. Park, Y.J. Shin, Solar Energy Mater. Solar Cells **95**, 179 (2011)
18. L. Shi, H. Lin, Langmuir **26**, 18718 (2010)
19. R. Demir-Cakan, Y.S. Hu, M. Antonietti, J. Maier, M.M. Titirici, Chem. Mater. **20**, 1227 (2008)
20. S. Fujihara, T. Maeda, H. Ohgi, E. Hosono, H. Imai, S.H. Kim, Langmuir **20**, 6476 (2004)
21. T. Krishnakumar, R. Jayaprakash, M. Parthibavarman, A.R. Phani, V.N. Singh, B.R. Mehta, Mater. Lett. **63**, 896 (2009)
22. M. Krishna, S. Komarneni, Ceram. Inter. **35**, 3375 (2009)
23. G.R. Patzke, Y. Zhou, R. Kontic, F. Conrad, Angew. Chem. Int. Ed. **50**, 826 (2011)
24. F. Gu, S.F. Wang, C.F. Song, M.K. Lu, Y.X. Qi, G.J. Zhou, D. Xu, D.R. Yuan, Chem. Phys. Lett. **372**, 451 (2003)
25. S.Y. Lee, Y.H. Shin, Y. Kim, S. Kim, S. Ju, J. Lumin. **131**, 2565 (2011)
26. D.J. Norris, M.G. Bawendi, Phys. Rev. B **53**, 16338 (1996)
27. E.M. Wong, P.C. Searson, Appl. Phys. Lett. **74**, 2939 (1999)
28. A. Sharma, S. Kumar, R. Kumar, M. Varshney, K.D. Verma, Adv. Mater. Rapid Commun. **3**, 1285 (2009)
29. D. Chen, L. Gao, J. Colloid Interface Sci. **279**, 137 (2004)
30. E.P. Domashevskaya, S.V. Ryabtsev, S.Y. Turishchev, V.M. Kashkarov, O.A. Chuvenkova, Y.A. Yurakov, Bull. Rus. Acad. Sci. Phys. **72**, 504 (2008)
31. F.A. Cotton, G. Wilkinson, *Advanced Inorganic Chemistry: A Comprehensive Text*, 4th edn. (Wiley-Interscience, USA, 1980), p. 393
32. K.L. Cheng, Microchem. J. **82**, 119 (2006)
33. Y. Shimizu, A. Jono, T. Hyodo, M. Egashira, Sens. Actuators B **108**, 56 (2005)
34. N. Savage, M.S. Diallo, Nanomaterials and water purification: opportunities and challenges. J. Nanoparticle Res. **7**, 331–342 (2005)
35. N. Yamazoe, G. Sakai, K. Shimanoe, Catal. Survey Asia **7**, 63 (2003)
36. A. Dieguez, A. Romano-Rodriguez, A. Vila, J.R. Morante, J. Appl. Phys. **90**, 1550 (2001)
37. S. Sarmah, A. Kumar, Ind. J. Phys. **84**, 1211 (2010)
38. S. Das, S. Kar, S. Chaudhuri, J. Appl. Phys. **99**, 1143030 (2006)
39. K. Vanheusden, W.L. Warren, C.H. Seager, D.R. Tallant, J.A. Voigt, B.E. Gnade, J. Appl. Phys. **79**, 7983 (1996)
40. S. Pokhrel, C.E. Simion, V.S. Teodorescu, N. Barsan, U. Weimar, Adv. Funct. Mater. **19**, 1767 (2009)
41. P. Sun, W. Zhao, Y. Cao, Y. Guan, Y. Sun, G. Lu, Cryst. Eng. Commun. **13**, 3718 (2011)
42. P.V. Kamat, R. Huehn, R.A. Nicolaescu, J. Phys. Chem. B **106**, 788 (2002)
43. D.E.D. Bois, US patent 4613845 (1986)